Computational Study of Subsonic Flow over a Delta Canard–Wing–Body Configuration

Ismail H. Tuncer* and Max F. Platzer†
U.S. Naval Postgraduate School, Monterey, California 93943

Subsonic flowfields over a close-coupled, delta canard–wing–body configuration at angles of attack of 20, 24.2, and 30 deg are computed using the OVERFLOW Navier–Stokes solver. Computed flowfields are presented in terms of particle traces, surface streamlines, and leeward-side surface pressure distributions for the canard-on and -off configurations. The interaction between the canard and the wing vortices, wing vortex breakdown, and the influence of the canard on vortex breakdown are identified. The comparison of the pressure data with the available experimental data at $Re = 0.32 \times 10^6$ and $Re = 1.4 \times 10^6$ shows a significant Reynolds-number dependence. Good agreement is obtained with the experiment for the canard-off configuration at all three angles of attack, and for the canard-on configuration at 20-deg angle of attack.

Introduction

THE flow over a close-coupled canard–wing–body config-uration at high angles of attack is highly complex because of flow separation, formation of canard and wing vortices and their interaction, and vortex breakdown. Studying the complex flowfield and understanding the effect of the canards on the performance, stability characteristics, and development of flow asymmetries are crucial to efforts in designing future aircraft and missile airframes. A recent comprehensive review of high-angle-of-attack aerodynamics has been given by Rom.[1] The present work is aimed at utilizing the current computational fluid dynamics (CFD) methods for studying the complex flowfields and validating the computed results with experimental data.

The canard–wing–body configuration was shown to in-crease the maximum lift coefficient and the corresponding an-gle of attack by constructive interaction between the canard and the wing vortices.[2] The interaction of the two vortex sys-tems strengthens the wing vortex and delays its breakdown. Hummel et al.[3,4] investigated experimentally the interaction be-tween the canard and delta wing vortices of a close-coupled delta canard configuration and showed that the breakdown of the delta wing vortices is delayed because of the presence of the canard vortices. They also traced vortex trajectories and determined the effect of the canard vortices on the surface pressure distribution over the wing.

Recent numerical computations[5-12] of flowfields around complete aircraft and missile configurations at high angles of attack show encouraging agreement with available experi-mental data. Tu[6,7] studied the transonic flow over a canard–w-ing–body configuration by means of the thin-layer Navier–Stokes equations. He calculated the strong effect of the canard vortex on the strength, reattachment, and separation of the wing vortex. He also calculated the effect of the canard on the surface pressure distribution. Similar solutions were performed by Ekaterinaris[8] for the configuration studied by Hummel et al.[3,4] at low subsonic speeds. He limited his anal-ysis to laminar flow computations for 20-deg incidence only, but confirmed the delay of vortex breakdown resulting from the canard and obtained good agreement with Hummel's data. Gutmark et al.[9,10] conducted a combined experimental and nu-merical study of a close-coupled canard–wing configuration. They compared pressure distributions over the wing and sur-face flow patterns with numerical computations and showed the strong effect of the canard on the flowfield over the wing over a wide range of angles of attack.

In this work, we build upon the previous work done by Ekaterinaris[8] and Gutmark et al.[9,10] The flowfields around the delta canard–wing–body (canard-on, Fig. 1) and wing–body configuration (canard-off) are computed using the OVER-FLOW thin-layer Navier–Stokes solver. The computed flow-fields are analyzed in terms of particle traces, surface stream-lines, and leeward-side surface pressure distributions. The computed surface pressure distributions on the wing, canard, and body are compared against available experimental data.

Numerical Method

The wing–canard–body configuration shown in Fig. 1 con-sists of a 60-deg swept delta canard and a delta wing with aspect ratios of 2.31. The canard and the wing are of sym-metric parabolic profiles in both chordwise and spanwise di-rections and have sharp leading edges. They are mounted co-planar on the midfuselage section with zero setting angles. This configuration is the same as the one employed in the experi-ments conducted by Hummel et al.[3,4] and Gutmark et al.[9,10]

In this study, only flows at zero sideslip angle are considered and the flowfield is assumed to be symmetric with respect to the midfuselage plane. Therefore, only the computational do-main around the half-fuselage canard–wing configuration is discretized by overset, structured subgrids. As shown in Fig. 2, six computational subgrids with a total number of approx-imately 1 million grid points are employed.[8] The canard and wing grids and the outer grids around them are relatively high-resolution grids with clustered grid points around the leading edges. The average grid spacing normal to the wing surface is $1 \times 10^{-5}c$ based on the wing chord length. Similarly, the av-erage grid size on the leeward side of the wing is about 0.01 and $0.03c$ in the crossflow and freestream directions, respec-tively. The PEGSUS code is used as a preprocessor to deter-mine the hole boundaries created by the overset grids in the outer grids and to localize the intergrid boundary points with interpolation stencils on the donor grid and the corresponding interpolation weights.

The OVERFLOW Navier–Stokes solver with multiblock, overset grids developed at NASA Ames Research Center,[5] is employed for the computation of the viscous, compressible flowfields. The OVERFLOW code has several discretization and time-integration schemes. In this study, for grids in which one of the (i, j, k) grid directions aligns with the freestream flow direction, the partial flux vector splitting algorithm is selected. Otherwise, the 3-factor diagonal scheme with central differencing is employed. The partial flux-vector-splitting algorithm uses Steger–Warming flux vector splitting for discretization of the convection terms in the streamwise direction, and central differencing in the other two directions. For the flux-splitting algorithm, the central difference smoothing coefficient was gradually reduced to about 0.06 from the starting value of 0.10. For the central-difference algorithm on the wing and canard grids the fourth-order smoothing coefficient was similarly reduced to 0.08 from 0.1. Local time stepping was used for convergence to a steady-state solution, and the convergence criteria was based on the L2 norm of the residuals and the variation of the aerodynamic loads on the wing and canard surfaces.

In this work we first computed laminar and fully turbulent flowfields at a low-Reynolds-number flow for comparison. In turbulent flow computations we employed the Baldwin–Barth one-equation turbulence model in all of the grids. Because the equation governing the turbulent eddy viscosity is solved in all of the grids with intergrid boundary conditions, the computed eddy viscosity is continuous across the grid boundaries as opposed to the discontinuous distribution in the Baldwin–Lomax algebraic eddy viscosity model.

All of the computations were carried out on remote Cray Y-MP and Cray C90 supercomputers. The FAST flow visualization software was used for postprocessing the flowfield data.

Results and Discussion

We computed flowfields for the canard-on and canard-off configurations at $\alpha = 20$, 24.2, and 30 deg; $M_\infty = 0.2$; and at

Fig. 4   Particle traces and surface streamlines. Turbulent flow at $\alpha = 20$ deg, $M_\infty = 0.2$, and $Re_C = 0.32 \times 10^6$

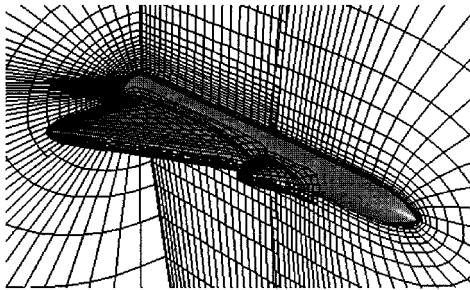**Fig. 1   Delta canard–wing–body configuration.**

Fig. 2   Overset computational grid (every other grid point is plotted).

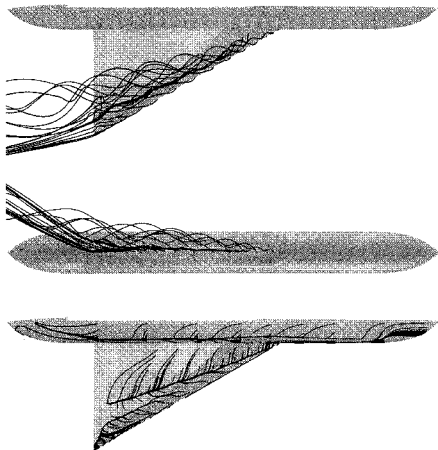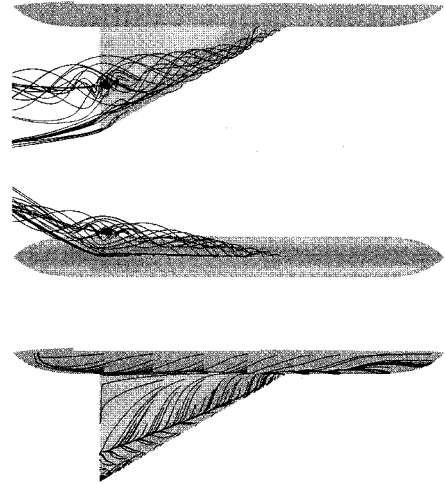**Fig. 3   Particle traces and surface streamlines. Laminar flow at $\alpha = 20$ deg, $M_\infty = 0.2$, and $Re_C = 0.32 \times 10^6$.**
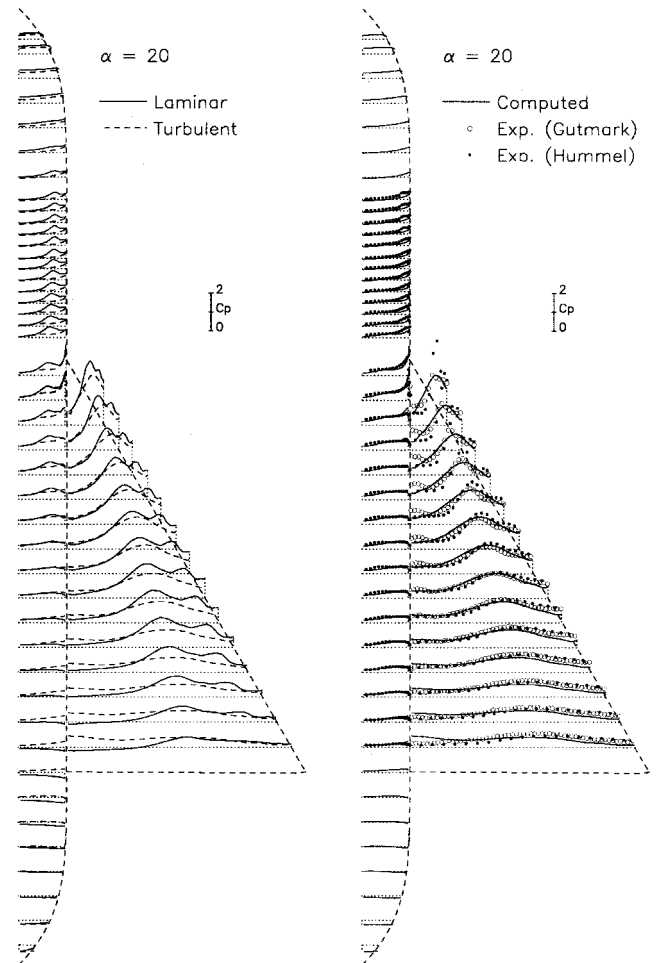
Fig. 5   Leeward-side surface pressure distribution. $\alpha = 20$ deg, $M_\infty = 0.2$, and $Re_C = 0.32 \times 10^6$.

two different Reynolds numbers Re_C = 0.32 × 10^6 or 1.4 × 10^6. The Reynolds number is based on the root-chord length of the wing. Computations with local time stepping for a single case took about 6000–10,000 time steps for convergence and 70–120 CPU hours on a Cray Y-MP. Convergence degraded significantly as the incidence angle increased. We analyzed the computed flowfields by means of particle traces shed from the leading edges of the wing and the canards, and the leeward-side surface streamlines. We also compared the leeward-side surface pressure distributions against the experimental data given by Gutmark et al.[9,10] and Bergmann et al.[4] for the same configurations at the matching Reynolds number. For this comparison, surface pressure values at the experimental data points were interpolated from the neighboring surface grid points after the data point is localized on the surface grid projected onto a two-dimensional surface. The localization of the experimental data points on the surface grid is based on an algorithm developed earlier for an overset grid solution method.[13]

The experiment by Gutmark et al.[9] was performed at the NASA Ames Research Center. The surface pressure distributions were obtained using pressure-sensitive, paint-measuring techniques[14] at M_∞ = 0.3 and Re_C = 0.32 × 10^6. They also employed a Mie scattering visualization technique for tracing the vortical flow and the vortex breakdown.

Hummel et al.[3,4] performed six-component aerodynamic load measurements, surface pressure measurements with pressure tabs, flowfield measurements using a five-hole probe, and flow visualization by means of oilflow patterns and a laser-lightsheet technique at M_∞ = 0.1, Re_C 1.4 × 10^6, and various incidences and sideslip angles.

The laminar and turbulent flowfields and surface pressure distributions computed for the canard-off configuration at α = 20 deg, Re_C = 0.32 × 10^6 are given in Figs. 3–5. It is readily observed that the laminar and turbulent flowfields differ significantly. The laminar solution predicts two strong vortices over the wing—the primary wing vortex and a secondary vortex—which induce suction peaks on the surface pressure distribution. The secondary and tertiary flow separation lines over the wing are also seen in the surface streamline patterns, which suggest the presence of a tertiary vortex. The laminar flow completely separates at the wing trailing edge as shown by the surface streamlines cut off at about 90% chord. It is also manifested by the pressure values higher than the freestream pressure at the inboard section of the wing. Moreover, it is also seen that the flow separates on the fuselage upstream of the wing, and forms a fuselage vortex. A secondary flow separation line is observed on the fuselage, and the suction peak trajectory on the body shown in Figure 5 suggests that a strong fuselage vortex initially develops.

In contrast to the laminar flowfield, in the turbulent flowfield predictions, the vortex flow over the wing remains attached until the trailing edge and the secondary vortex remains relatively weak as depicted by the absence of a secondary suction peak in the pressure distribution. The primary vortex core and the induced suction trajectories are closer to the leading edge. Incidentally, the surface pressure distribution on the wing in general agrees remarkably well with the experimental data. In the experimental data the increased suction at the forward wing-fuselage junction is caused by the presence of a small gap at the junction, where a jet-like flow develops, originating from the bottom surface. It is also observed in Fig. 4 that the primary wing vortex breaks down at about 90% chord location as shown in the particle traces. The vortex breakdown was captured by first scanning the computational domain for diminishing axial velocity and then by particle traces originating at the corresponding locations. In the experiments, although it was not conclusive, the vortex breakdown location is predicted downstream of the 80% chord location.[8]
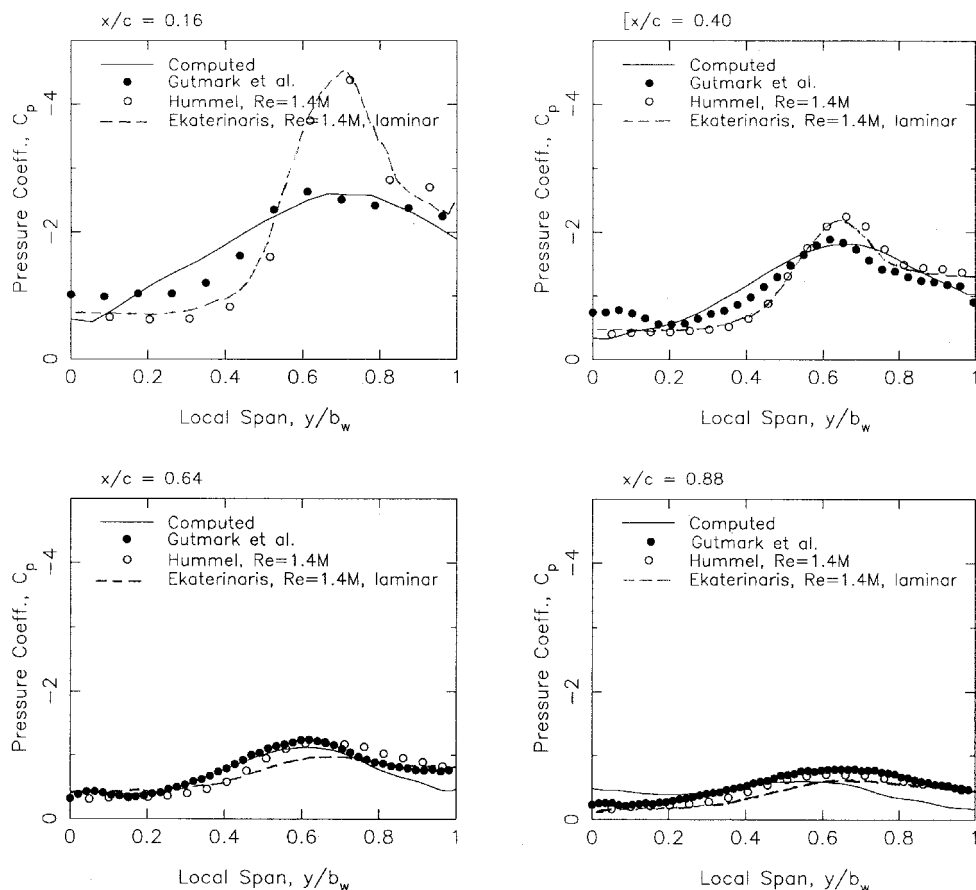

Fig. 6   Leeward-side wing surface pressure distribution. Canard-off configuration, α = 20 deg, M_∞ = 0.2, and Re_C = 0.32 × 10^6.

In Fig. 6 the measured and computed spanwise pressure distributions on the wing are shown in detail at four chordwise stations, x/c = 0.16, 0.4, 0.64, and 0.88. It is readily seen that there are significant differences between the measured distributions at the Reynolds numbers of 0.32×10^6 and 1.4×10^6 on the forward part of the wing at x/c = 0.16 and 0.4. This difference can be partially explained by the presence of a small gap between the fuselage and the wing in the model tested by Gutmark et al.[9,10] The effect of this gap is visible in the pressure distribution near the fuselage at x/c = 0.4. However, most of the differences must be attributed to the difference in Reynolds number, which appears to produce a weaker vortex and therefore a smaller suction peak at the lower-Reynolds-number case. Using a laminar flow calculation, Ekaterinaris[8] obtained remarkably good agreement with Hummel's experimental results[3] at Re_C = 1.4×10^6. Our turbulent flow computations at Re_C = 0.32×10^6 agree fairly well with the measurements of Gutmark et al.,[9,10] except near the fuselage.

The flowfields for the canard-on configuration at α = 20 deg are shown in Figs. 7–9. In addition to the different trends between laminar and turbulent flowfields observed earlier, in the presence of the canard the laminar flowfield stalls over the fuselage and over a large portion of the wing and pressure values larger than freestream pressure are predicted. The interaction between canard and wing vortices is also less pronounced in the laminar flowfield as the canard vortex is pushed inboard by the wing vortex sidewash. Whereas in the turbulent flowfield there is a stronger interaction between the canard and

wing vortices, and the canard vortex merges into the wing vortex. The combined vortex is then pushed farther outboard as compared to the canard-off case. The wing vortex breakdown appears to be eliminated completely and the vortex suction over the wing is preserved off of the trailing edge. The wing surface pressure distribution again agrees remarkably well with the experimental data for the turbulent flow computations. Figure 10 similarly shows a comparison of the measured and computed spanwise wing pressure distributions in detail. A significant Reynolds number effect is again observed. In fact, the measurements of Gutmark et al.[9,10] show no enhanced suction peak because of the presence of the canard at Re_C = 0.32×10^6. However, our turbulent flow calculations are again in fairly good agreement with the measurements, except near the fuselage because of the gap effect, as noted earlier.

The computed turbulent flowfield predictions for the canard-on and canard-off configurations at α = 24.2 deg and Re_C = 1.4×10^6 are shown in Figs. 11–13. The flowfields closely resemble those at α = 20 deg, except that in the canard-off configuration the vortex breakdown now occurs at about 75% chord location and the secondary flow separation lines on the wing and the canard surfaces move farther outboard toward the leading edge. This is attributed to the downwash induced by a stronger vortex, which is also manifested in the surface pressure distribution by the greater suction peak. The wing vortex is also lifted farther up from the surface. Similar to the α = 20-deg case, the primary vortex breakdown is not observed in the canard-on configuration. On the other hand, in the experiment[4] the vortex breakdown locations are denoted approximately at the 30 and 70 chord locations for canard-off and -on configurations, respectively. Although the vortex breakdown
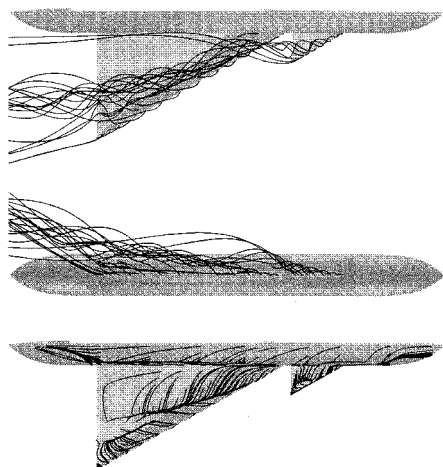

Fig. 7   Particle traces and surface streamlines. Laminar flow at α = 20 deg, M_∞ = 0.2, and Re_C= 0.32×10^6.
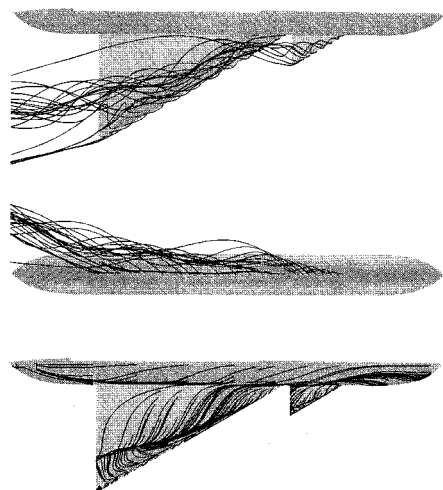

Fig. 8   Particle traces and surface streamlines. Turbulent flow at α = 20 deg, M_∞ = 0.2, and Re_C= 0.32×10^6.
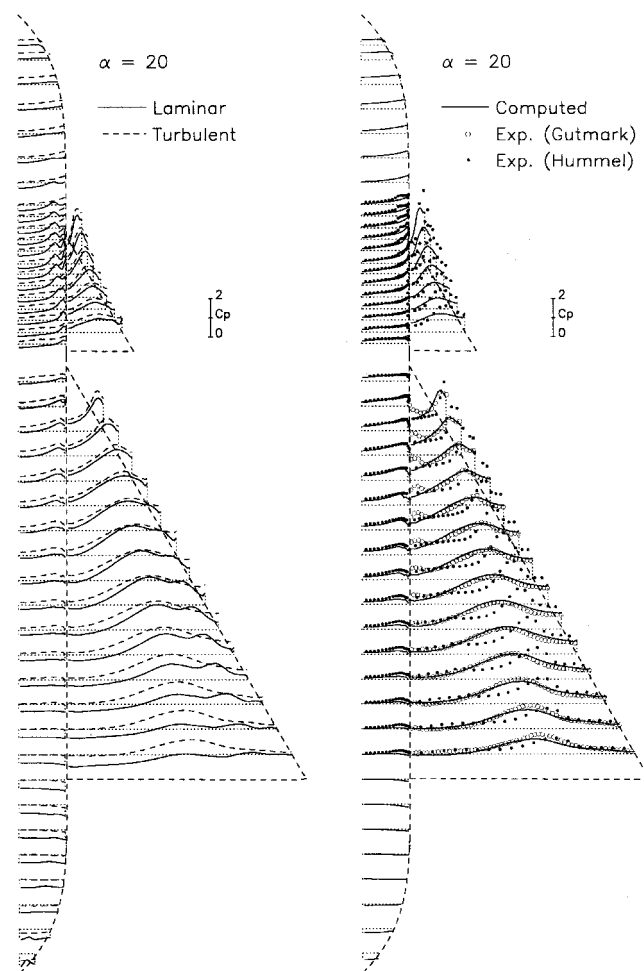

Fig. 9   Leeward-side surface pressure distribution. α = 20 deg, M_∞ = 0.2, and Re_C= 3.2×10^5.
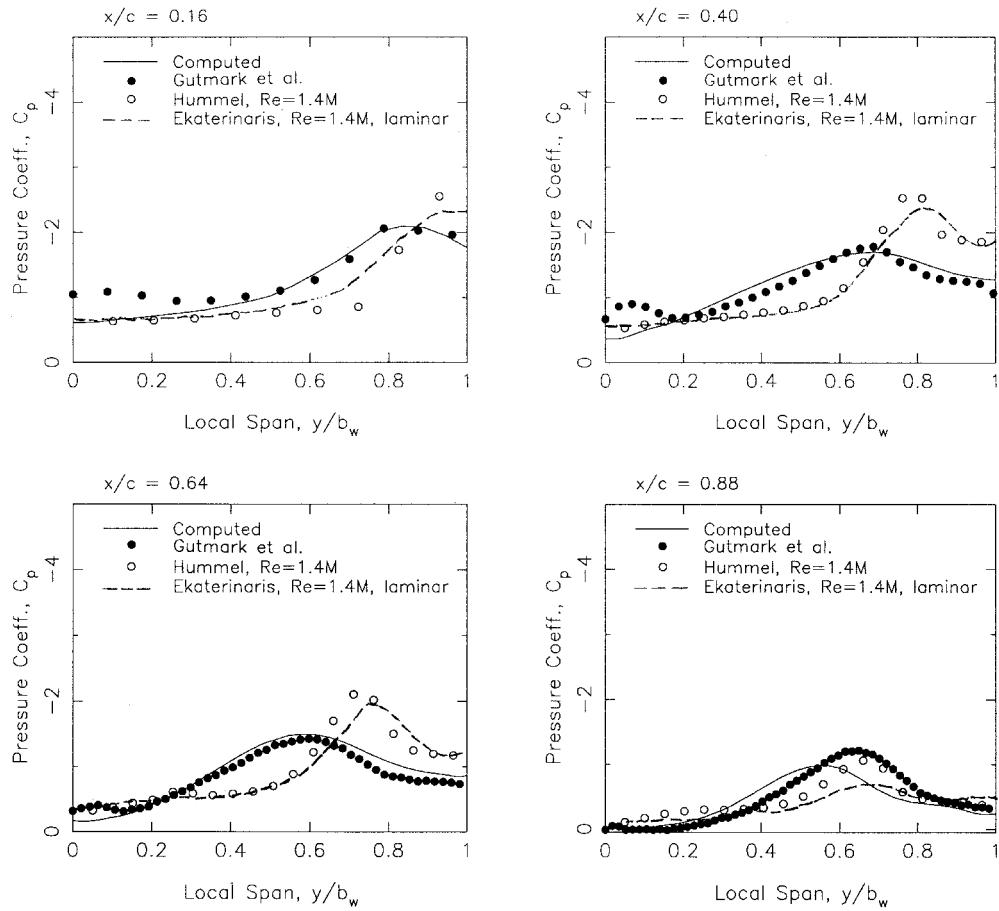
Fig. 10   Leeward-side wing surface pressure distribution. Canard-on configuration, α = 20 deg, M_∞ = 0.2, and Re_C= 0.32 × 10⁶.
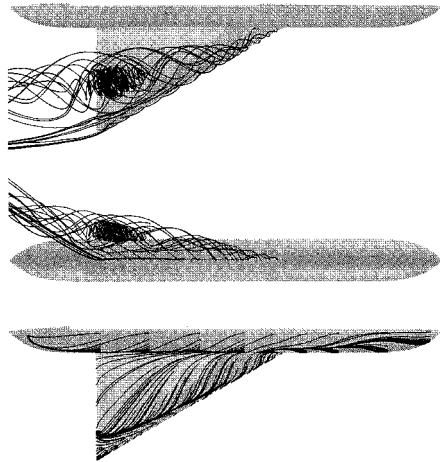

Fig. 11   Particle traces and surface streamlines. Turbulent flow at α = 24.2 deg, M_∞ = 0.2, and Re_C= 1.4 × 10⁶.

Fig. 12   Particle traces and surface streamlines. Turbulent flow at α = 24.2 deg, M_∞ = 0.2, and Re_C= 1.4 × 10⁶.

locations are significantly different, the surface pressure distribution in the canard-off case agrees quite well with the experimental data. However, in the canard-on configuration, the pressure distributions and the wing vortex suction peak trajectories differ significantly. It is reported in the experiment that the canard vortex preserves its core over the wing. The separate presence of the canard vortex therefore significantly pushes the wing vortex toward the leading edge, which is clearly seen in the experimental surface pressure distributions in Fig. 11. In contrast, in the computations the interaction between the vortices is much stronger and the canard vortex is completely engulfed into the wing vortex. The canard vortex appears to be highly diffused and not resolved sufficiently in the present computations. It might be
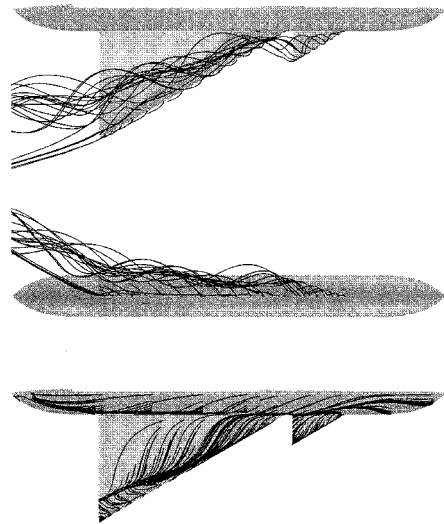
speculated that because a strong vortex core is not preserved, it gets engulfed by the wing vortex.

At α = 30 deg, flowfields are computed at Re_C = 1.4 × 10⁶ and 0.32 × 10⁶ for the canard-off and canard-on configurations, respectively (Figs. 14–16). Figure 17 shows the comparisons of the spanwise wing pressure distributions for the canard-on configuration in detail. Again, the experimental results indicate that there is a substantial Reynolds-number effect. Both, Ekaterinaris' laminar high-Reynolds-number[8] and our turbulent low-Reynolds-number computations differ significantly from the
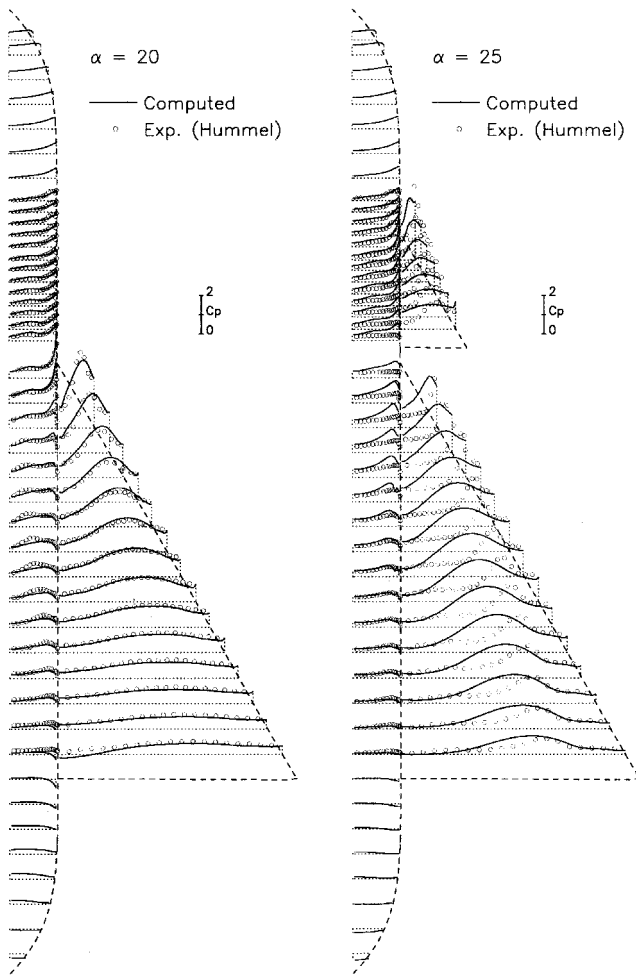
Fig. 13   Leeward-side surface pressure distribution. Turbulent flow at α = 24.2 deg, M_∞ = 0.2, and Re_C = 1.4 × 10⁶.
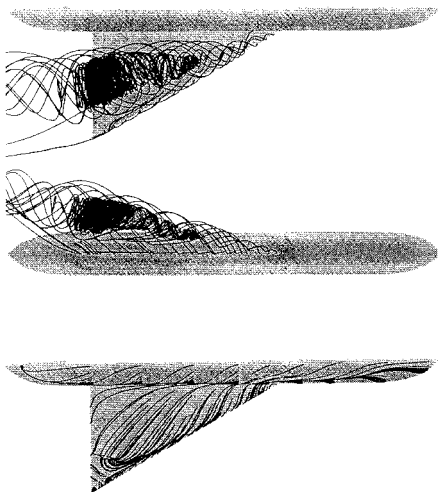

Fig. 14   Particle traces and surface streamlines. Turbulent flow at α = 30 deg, M_∞ = 0.2, and Re_C = 1.4 × 10⁶.

Fig. 15   Particle traces and surface streamlines. Turbulent flow at α = 30 deg, M_∞ = 0.2, and Re_C = 0.32 × 10⁶.

Fig. 16   Leeward-side surface pressure distribution. Turbulent flow at α = 30 deg, M_∞ = 0.2, and Re_C = 1.4 × 10⁶ for canard-off configuration, and Re_C = 0.32 × 10⁶ for canard-on configuration.

measurements. In the canard-off configuration, as the vortical flow lifts off the wing surface, the secondary flow separation line on the wing moves much closer to the leading edge. Incidentally, the vortex breakdown occurs at about 40% chord location. Although in Hummel's experiment[3,4] at α = 29.1 deg, the vortex breakdown location is depicted at about 15% chord location, the computed surface pressure distribution agrees well
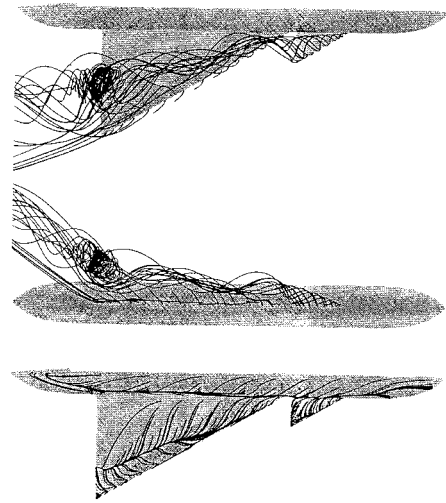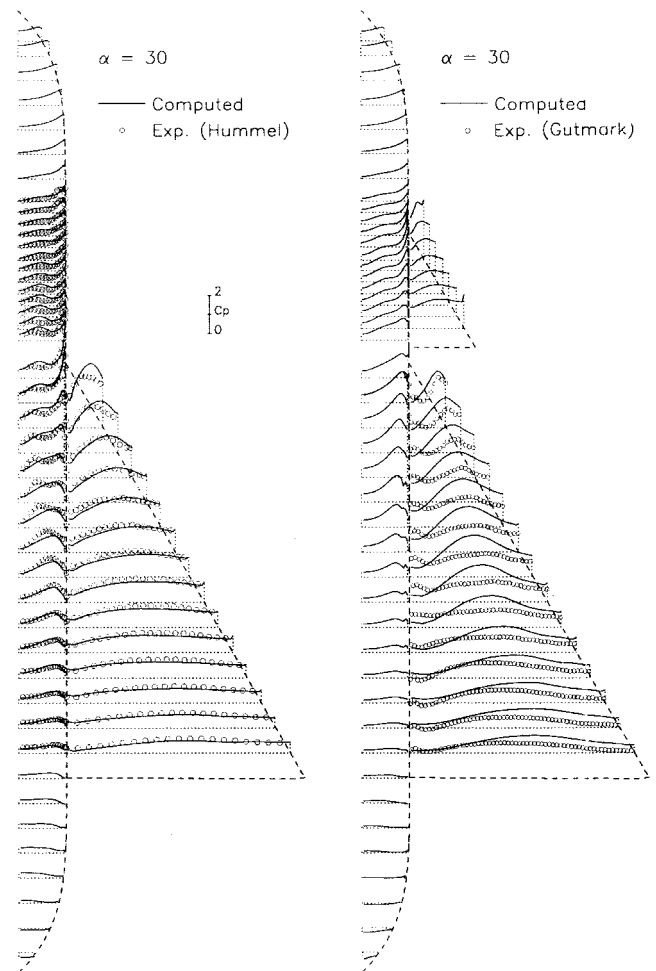
with the experimental data. In the canard-on configuration, at the lower-Reynolds-number flow, the vortex breakdown is now observed at the trailing edge. However, there are again significant differences between the computed and the experimental surface pressure distributions. In the experiments the vortex breakdown appears to occur closer to the apex and the suction field on the wing collapses earlier.
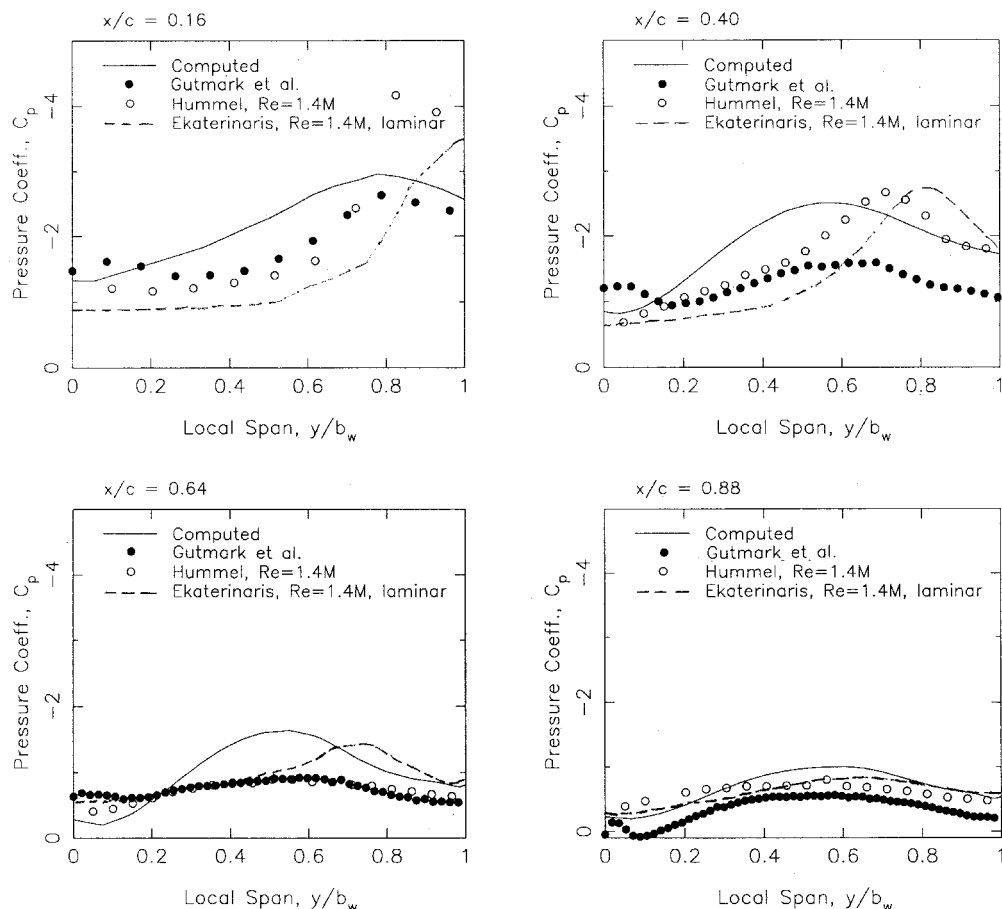
Fig. 17   Leeward-side wing surface pressure distribution. Canard-on configuration, $\alpha = 30$ deg, $M_\infty = 0.2$, and $Re_C = 0.32 \times 10^6$.

Concluding Remarks

A thin-layer Navier–Stokes solver with overset grids, OVER-FLOW, was employed to compute the subsonic flow over fuselage–wing and fuselage–canard–wing configurations at high angles of attack from 20 to 30 deg. The available experimental results show that there is a significant Reynolds-number influence. Using a fully turbulent flow computation it was found that the flowfield and the pressure distribution on the fuselage–wing configuration could be predicted fairly well. However, the prediction of the flow over the close-coupled fuselage–canard–wing configuration presents a far more challenging problem. Here, reasonable agreement could be obtained only at 20-deg angle of attack. It appears that in the computations the strong interaction between the canard and wing vortices is not resolved accurately at higher angles of attack. Further experimental and computational work is necessary to study the complicated vortical flow interactions that occur at higher angles of attack.

Acknowledgments

References

[1]Rom, J., *High Angle of Attack Aerodynamics*, Springer–Verlag New York, 1992.

[2]Behrbohm, H., "Basic Low Speed Aerodynamics of the Short-Coupled Canard Configuration of Small Aspect Ratio," SAAB Aktiebolag, TN 60, Linkoeping, Sweden, 1965.

[3]Hummel, D., and Oelker H.-C., "Vortex Interference Effects on Close-Coupled Canard Configuration at Low Speed," *Aerodynamics of Combat Aircraft Controls and of Ground Effects*, CP-465, AGARD, 1989, pp. 7-1–7-18.

[4]Bergmann, A., Hummel, D., and Oelker H.-C., "Vortex Formation over a Close-Coupled Canard-Wing-Body Configuration in Unsymmetrical Flow," *Vortex Flow Aerodynamics*, CP-494, AGARD, 1990, pp. 1–14.

[5]Ying, S. X., Steger, J. L., Schiff, L. B., and Baganoff, D., "Numerical Simulation of Unsteady, Viscous High-Angle-of-Attack Flows Using a Partially Flux-Split Algorithm," AIAA Paper 86-2179, Aug. 1986.

[6]Tu, E. L., "Navier-Stokes Simulation of a Close-Coupled Canard-Wing-Body Configuration," *Journal of Aircraft*, Vol. 29, No. 5, 1992, pp. 830–838.

[7]Tu, E. L., "Effect of Canard Deflection on Close-Coupled Canard-Wing-Body Aerodynamics" *Journal of Aircraft*, Vol. 31, No. 1, 1994, pp. 138–145.

[8]Ekaterinaris, J. A., "Analysis of Flowfields over Missile Configurations at Subsonic Speeds," *Journal of Spacecraft and Rockets*, Vol. 32, No. 3, 1995, pp. 385–391.

[9]Gutmark, E. J., Yu, K., VanDyken, R. D., Tuncer, I. H., and McLachlan, B. G., "Experimental and Computational Study of Canard-Wing-Body Configuration at High Angle-of-Attack," AIAA Paper 95-1863, June 1995.

[10]VanDyken, R. D., Gutmark, E. J., Yu, K., Tuncer, I. H., Platzer, M. F., and McLachlan, B. G., "Passive and Active Control of Flow Separation over Delta Wings at High Angle-of-Attack," AIAA Paper 96-0661, Jan. 1996.

[11]Tuncer, I. H., Marvin, R., and Platzer, M. F., "Numerical Investigation of Subsonic Flow over a Typical Missile Forebody," AIAA Paper 96-0189, Jan. 1996.

[12]Tuncer, I. H., Platzer, M. F., and VanDyken, R. D., "A Computational Study of Subsonic Flowfields over a Missile Configuration," AIAA Paper 97-0635, Jan. 1997.

[13]Tuncer, I. H., "A 2-D Navier-Stokes Solution Method with Overset Grids," American Society of Mechanical Engineering, Paper 96-GT-400, June 1996.

[14]McLachlan, B. G., Bell, J. H., Kennelly, R. A., Schreiner, J. A., Smith, S. C., and Strong, J. M., "Pressure Sensitive Paint Use in the Supersonic High-Sweep Oblique Wing Test," AIAA Paper 92-2686, June 1992.